Journal of
Materials Chemistry C

ROYAL SOCIETY
OF CHEMISTRY

PAPER

View Article Online
View Journal | View Issue

Check for updates

Cite this: *J. Mater. Chem. C*, 2025, **13**, 6779

Fabrication of loss-less $La_3Si_6N_{11}:Ce^{3+}$ phosphor-in-glass color converters using oxygen-free ZIF-62 glass†

Taoli Deng,[a,b] Zan Ding,[c] Shuang Zheng[b] and Rong-Jun Xie *[b]

Received 20th December 2024,
Accepted 10th February 2025

DOI: 10.1039/d4tc05380j

rsc.li/materials-c

Ce^{3+}-doped nitride phosphors are promising color converters in laser-driven lighting and display technologies, but they suffer from serious loss in luminescence efficiency caused by the interfacial reaction between phosphor powders and glass powders during the fabrication of phosphor-in-glass bulks or films. In this work, the oxygen-free organic–inorganic hybrid glass (OIHG) $Zn(Im)_3(HbIm)$ (ZIF-62) was used instead of the traditional oxide glass to prepare an $La_3Si_6N_{11}:Ce^{3+}$ (LSN) phosphor converter by cofiring LSN with the ZIF-62 glass. The LSN phosphor-in-ZIF-62 glass converter well maintains the internal quantum efficiency of the original phosphor powders, showing a luminescence loss of only ~1%. The sandwich-structured LSN-in-ZIF-62 glass converter, constructed by cofiring it with sapphire substrates, enables the generation of white lighting with a maximum luminous flux of 872.2 lm and a luminous efficacy of 291 lm W^{-1} when pumped by a blue laser diode at a powder density of 5.99 W mm^{-2}. The use of the oxygen-free ZIF-62 glass provides a viable method to design nitride phosphor-based color converters for low-power laser-driven lighting, high-power LED lighting or projection applications.

1. Introduction

Laser-driven solid-state lighting, achieved by pumping phosphor converters with blue laser diodes, promises super-brightness and high-collimation white-lighting sources and has led to the development of next-generation lighting and display technologies.[1–9] In this emerging technology, a phosphor converter is one of the key components to control the optical quality and service time of lighting sources, but the design of phosphor converters with excellent optical properties that can be retained after high-power-density laser excitation is still a significant challenge. Among many types of phosphors, nitride phosphors have received great attention owing to their outstanding thermal stability and structural rigidity, which make them promising converters in laser-driven lighting and display technologies.[10–16]

Currently, phosphor-in-glass (PiG) color converters are commonly used for laser lighting because they are easily prepared and inexpensive compared to their counterparts such as single crystals and phosphor ceramics.[17–20] However, it is difficult to prepare highly efficient nitride-PiG converters because nitride phosphor powders usually react with glass powders at firing temperatures, and their photoluminescence properties are then largely quenched (Table S1, ESI†).[12,21–24] Therefore, cofiring nitride phosphors with glass powders into dense PiG color converters is an interesting topic but a difficult task that needs to be further investigated.

$La_3Si_6N_{11}:Ce^{3+}$ (LSN) is an excellent yellow-green phosphor with high quantum efficiency (QE) and thermal stability, and its emission can be redshifted through partial substitution of La with Y (*i.e.*, LYSN).[25] We prepared LSN-PiG and LYSN-PiG films and used them to produce high-brightness white and warm white laser lighting, respectively.[12,26] However, the loss in the QE of LSN or LYSN is not inevitably avoided because the nitride phosphor powders react with the melting oxide glass during cofiring. Although the oxidation reaction was effectively alleviated by uniformly coating the phosphor particles with hexagonal boron nitride (BN) to isolate the nitride phosphors from the glass matrix, the internal quantum efficiency (IQE) of the LYSN-BN PiG films was still declined by 7.9% when compared to that of the original LYSN phosphor (*i.e.*, 77.9% → 70%). Therefore, it is necessary to find oxygen-free glass to totally prevent the reaction between phosphor and glass powders.

As we may know, the traditional glass can be mainly categorized into three types, namely, inorganic glasses, organic glasses and metallic glasses. They are dominated by mixed

---

[a] *College of Chemistry and Chemical Engineering, Anshun University, Anshun 561000, P. R. China*
[b] *Fujian Key Laboratory of Surface and Interface Engineering for High Performance Materials, College of Materials, Xiamen University, Xiamen 361005, P. R. China. E-mail: rjxie@xmu.edu.cn*
[c] *Guizhou University, Guiyang 550000, P. R. China*

† Electronic supplementary information (ESI) available. See DOI: **https://doi.org/10.1039/d4tc05380j**

ionic-covalent bonds, covalent bonds and metallic bonds, respectively. The organic–inorganic hybrid glass (OIHG), considered as the fourth category of melt-quenched glasses, includes metal–organic framework (MOF) crystals, coordination polymers (CPs), metal–organic–inorganic complexes (MOCs) and metal coordination compounds (MCCs), which have recently demonstrated potential uses in gas separation, energy storage and optics application.[27–35] The OIHG presents a novel pathway for fabricating bulk functionalized structural materials, and its application in optical fields has been reported. For instance, Bennett *et al.* prepared the melt-quenched glass ZIF-62 of halide perovskites by liquid-phase sintering and found that the glass retained the exceptionally high efficiency of halide perovskite quantum dots and exhibited remarkable optical stability under various environmental conditions.[36–38] Qiu *et al.* successfully designed a variety of bulk optical materials based on MOCs combined with dyes and phosphors, which also demonstrate outstanding optical properties.[28,31]

In this work, to address the issue of oxidation-induced QE loss when nitride phosphors are cofired with traditional glasses, the OIHG, which can provide the oxygen-free sintering environment, was first synthesized and then cofired with nitride phosphor powders to form nitride-PiG films without luminescence loss as far as possible. The design of the nitride-PiG films by using the OIHG paves a way for applying nitride phosphor converters in low-power laser-driven lighting and displays, as well as high-power LED lighting.

2. Experimental section

2.1. Fabrication of nitride-PiG bulks using the ZIF-62 OIHG

2.1.1. Materials. The phosphor of $La_3Si_6N_{11}:Ce^{3+}$ (LSN:Ce, Mitsubishi Chemical Co., Ltd., Japan) was commercially available. Zinc nitrate hexahydrate ($Zn(NO_3)_2{\cdot}6H_2O$, Aladdin Reagent Co., Ltd., China), imidazole (Im, Aladdin Reagent Co., Ltd., China), benzimidazole (HbIm, Aladdin Reagent Co., Ltd., China), dimethylformamide (DMF, Aladdin Reagent Co., Ltd., China) and dichloromethane (DCM, Aladdin Reagent Co., Ltd., China) were all purchased. Single-crystal sapphire plates with a size of $14 \times 14 \times 1\ mm^3$ were bought from the Yuanfeng Quartz Products Co. Ltd. (China).

First, $Zn(NO_3)_2{\cdot}6H_2O$, Im and HbIm in a molar ratio of 3 : 25 : 5 were added into 100 mL DMF. Then, the mixture was stirred at room temperature for 30 min and subsequently transferred to a reaction autoclave for hydrothermal treatment. The treatment was done at 130 °C for 60 h. Second, the reaction solution was centrifuged and filtered to obtain white crystalline powders, followed by washing with the DMF solution for three times and with DCM for two times. The washed white crystalline powders were activated in a tubular furnace under vacuum at 150 °C for 72 h to complete the evaporation of residual DMF and DCM, and then the $Zn(Im)_3(HbIm)$ (ZIF-62) powders were obtained.

ZIF-62 powders were thoroughly mixed with LSN:Ce phosphors in a certain molar mass ratio. Specifically, the mass ratio of ZIF-62 to LSN:Ce was set at 2/1, 1/1, 3/2 and 1/2. Then the mixed powders were pressed into a circular bulk under a pressure of ~0.1 MPa, with sapphire plates attached to both the top and bottom surfaces to construct a sandwich-structured phosphor converter. The sapphire plates were clamped with four stainless steel clips (*i.e.*, an approximate force of 200 N was applied). The assembled phosphor converter was placed in a tubular furnace and heated to the desired temperatures (*i.e.*, 370, 380, 390 and 400 °C) at a rate of 10 °C min^{-1} in an Ar atmosphere. The holding time was 15 min. Then, the sample was cooled naturally to room temperature to finally obtain the LSN-in-ZIF-62 glass converter. The detailed fabrication procedure of the sandwich-structured LSN-in-ZIF-62 converter is illustrated in Fig. 1a.

2.2. Characterizations

The phase compositions of the ZIF-62 crystal, ZIF-62 glass and the LSN-in-ZIF-62 glass converters were characterized using an X-ray diffractometer (D8 Advanced, Bruker, Germany) with Cu Kα radiation at 40 kV and 40 mA. The microscopic morphology and elemental distribution mapping were obtained using an energy-dispersive spectroscope (EDS, X-MaxN, Oxford, UK) coupled with a field emission scanning electron microscope (SEM, SU70, Hitachi, Japan). Fluorescence microscopic images of the LSN-in-ZIF-62 glass were recorded using a fluorescence microscope (DP74, OLYMPUS, Japan). The transmittance of the ZIF-62 glass was measured using an ultraviolet-visible spectrophotometer (UV 3600 Plus, Shimadzu Corporation, Japan). The thermogravimetric (TG) analysis and DSC curves of the ZIF-62 crystal and glass were acquired using a simultaneous thermal analyzer (STA, 449 F3 Jupiter, Netzsch, Germany). The infrared spectra of the ZIF-62 crystal and glass were measured using an infrared spectrometer (Nicolet is10, Thermo Fisher, USA).

Temperature-dependent emission spectra of the LSN-in-ZIF-62 glass converters were measured at temperatures ranging from 298 to 548 K using a system with a 450 nm LED light source, a charge-coupled device (CCD) spectrometer (USB2000 +, Ocean Optics, USA), and a cooling-heating stage (THMS600E, Linkam, UK). The IQE of all samples was determined by a system consisting of an excitation light source (450 nm, 50 mW blue laser diode), an integrating sphere (diameter of 15 cm), and a CCD spectrometer (USB2000 +, Ocean Optics, USA). The optical properties of the LSN-in-ZIF-62 glass converters under blue laser excitation were measured in a static reflective configuration using a sphere-spectroradiometer system, as shown in Fig. 1b, which consists of a blue laser light source with an area of 0.5 mm^2 (LSR445CP-FC-48W, Lasever, China), an integrating sphere (diameter of 30 cm), and a CCD spectrometer (HR4000, Ocean Optics, USA).

3. Results and discussion

3.1. Microstructure and properties of organic–inorganic hybrid glass ZIF-62

The ZIF-62 crystals were acquired by a hydrothermal method and further processed into an OIHG by a sintering process. The

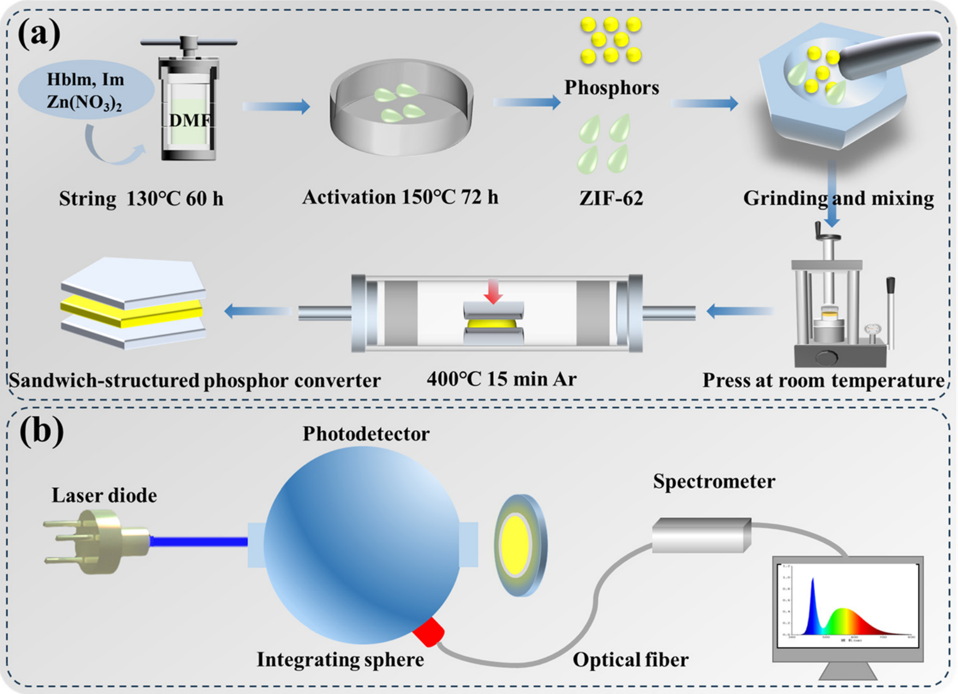

Fig. 1 (a) Fabrication procedure of the sandwich-structured LSN-in-ZIF-62 glass converter. (b) Schematics of the optical property measurement for the LSN-in-ZIF-62 glass converters under laser excitation.

XRD pattern of ZIF-62 crystals presents sharp peaks, indicating a highly ordered crystalline structure, as evidenced in Fig. 2a, and these peaks match well with the simulated diffraction pattern of the ZIF-62 crystals.[39] All characteristic diffraction peaks disappear after the ZIF-62 crystal is transformed into the ZIF-62 glass. The SEM image of the ZIF-62 crystal (Fig. 2b) shows that the crystal possesses a block-like morphology with well-defined edges and a notably uniform particle distribution with a size of 10–20 μm. Further, the EDS mapping corroborates that the elements Zn, N and C are uniformly dispersed throughout the ZIF-62 crystals, as presented in Fig. 2c–f.

The sintering process of the OIHG is crucial for preparing the PiG converter. First, the tablet-shaped ZIF-62 crystals clamped with four stainless steel clips were sintered at 370, 380, 390 and 400 °C for 15 minutes in an Ar atmosphere. The actual photos of the sintered ZIF-62 glass are given in Fig. 3a. When the sintering

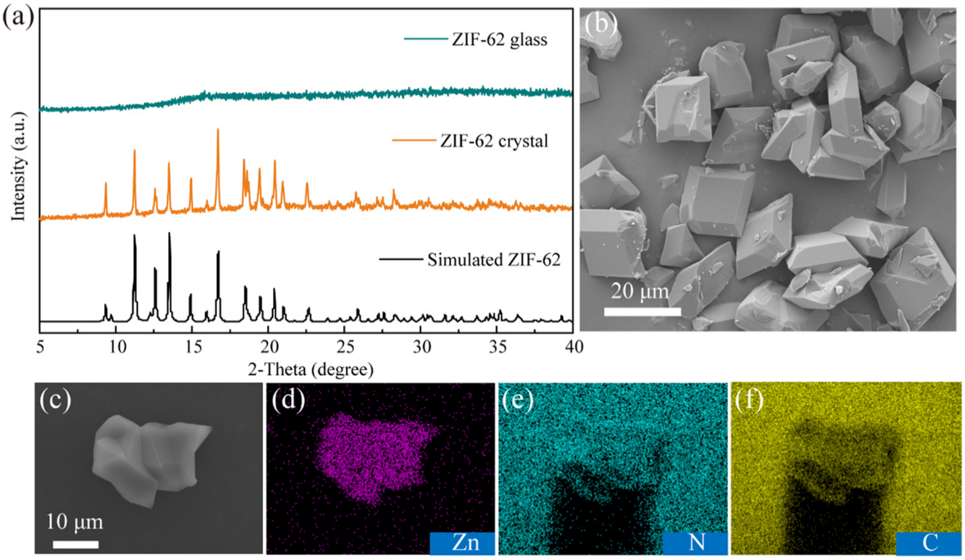

Fig. 2 (a) XRD patterns of the ZIF-62 crystal and glass. (b) SEM image of the ZIF-62 crystals. (c)–(f) Corresponding EDS mappings of Zn, N, and C elements.

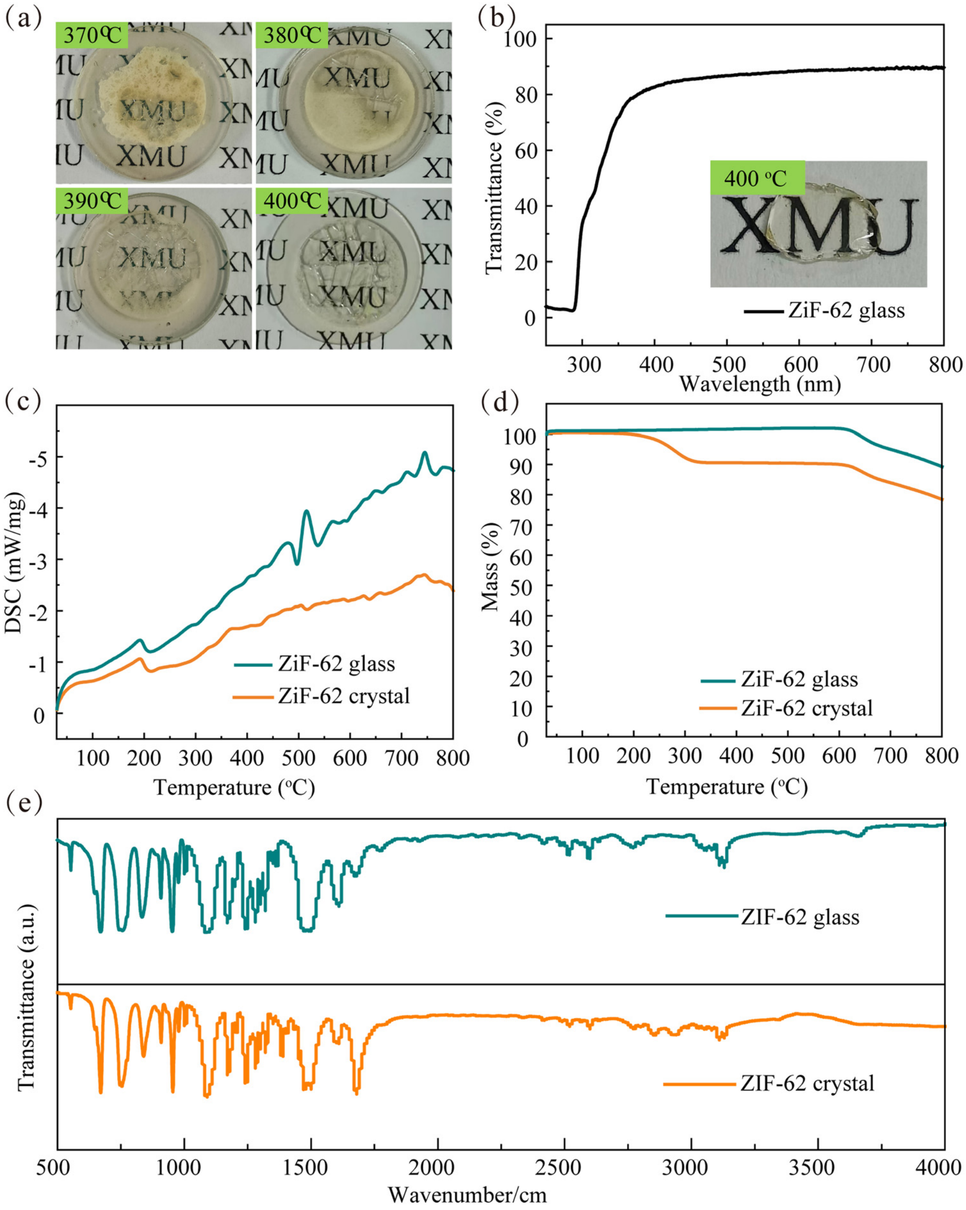

Fig. 3 (a) Photographs of the ZIF-62 glasses sintered at different temperatures. (b) Transmittance spectrum of the ZIF-62 glass sintered at 400 °C. (c) DSC curves of the ZIF-62 crystal and ZIF-62 glass. (d) TG curves of the ZIF-62 crystal and ZIF-62 glass. (e) Infrared spectra of the ZIF-62 crystal and ZIF-62 glass.

temperature is 370 °C, only a small area in the middle appears transparent. The transmittance of the ZIF-62 glass is greatly enhanced and a large area turns transparent when the sintering temperature is further increased. After sintering at 400 °C for 15 min, the ZIF-62 glass shows a transmittance as high as ~87% in the visible light region (400–800 nm), which matches well with both the blue laser light and the converted light to improve the light extraction efficiency. The transmittance shows a dramatic drop below 400 nm (Fig. 3b).

The DSC and TG curves of the ZIF-62 crystals and ZIF-62 glass are presented in Fig. 3c and d, and it can be observed that the T_g value of the ZIF-62 glass appears at 515 °C, followed by the onset of T_f at 715 °C. In contrast, the DSC curve of the ZIF-62 crystals is relatively smooth, indicating the absence of phase transition or crystallization. Further, the TG curves of the ZIF-62 crystals and ZIF-62 glass reveal that the thermal decomposition of the ZIF-62 crystals slowly occurs. Below 200 °C, there is virtually no mass loss, followed by a mass loss of approximately 12% between 200 °C and 600 °C. Subsequently, an additional mass loss occurs above 600 °C, with the sample retaining 75% of its original mass at 800 °C. However, the ZIF-62 glass exhibits remarkable thermal stability, with a negligible mass loss up to 580 °C. Fig. 3e shows the infrared spectra of the ZIF-62 crystal and ZIF-62 glass. All functional group vibration characteristic peaks of both the ZIF-62 crystal and glass are at the same position, indicating that there is no chemical bond breakage or formation during the transformation of the ZIF-62 crystal into the ZIF-62 glass.

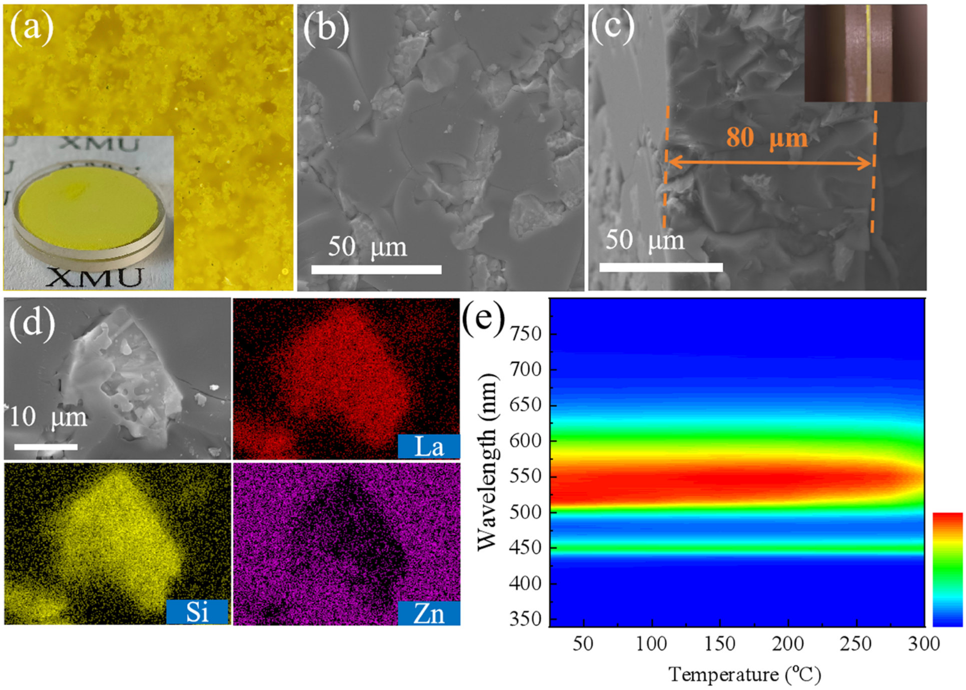

Fig. 4 (a) Fluorescence microscopic image (the inset is the photograph of the converter). (b) Top-view SEM image and (c) cross-section SEM image of the LSN-in-ZIF-62 glass converter (the inset is the photograph of the cross-section of the converter). (d) Corresponding EDS mappings of La, Si and Zn elements. (e) Temperature-dependent emission spectra of the glass converter.

3.2. Optical properties of the LSN-in-ZIF-62 glass converters

Owing to the high transmittance and strong thermal stability of the ZIF-62 glass, a novel LSN-in-ZIF-62 glass converter was prepared. It can be seen from the photos that the glass converter has a flat surface and uniform color. Further, the fluorescence microscopic image of the LSN-in-ZIF-62 glass converter shows that the LSN:Ce phosphor particles are evenly dispersed in the glass matrix, as shown in Fig. 4a and b. A few pores are also seen in the glass matrix. The thickness of the LSN-in-ZIF-62 glass converter is ~80 μm determined from the cross-section SEM image shown in Fig. 4c. The SEM-EDS spectra demonstrate the distribution of the major elements La and Si from the phosphor particles, and Zn from the glass in the converter. A clear boundary between the LSN:Ce particle and the glass matrix is observed, indicating that no significant interfacial reaction occurs during the sintering process (Fig. 4d). In addition, the XRD pattern of the LSN-in-ZIF-62 glass converter is presented in Fig. S1 (ESI†). After the transformation of the ZIF-62 crystal into glass, all of the crystal characteristic diffraction peaks disappear, while the remaining major diffraction peaks can be matched well with the standard card of LSN phase (ICSD 248709).[12] It is worth noting that the LSN-in-ZIF-62 glass converter presents an outstanding thermal stability, which can maintain the photoluminescence intensity of over 90% at 250 °C (Fig. 4e).

The optical properties of the LSN-in-ZIF-62 glass converter with different mass ratios of the ZIF-62 glass to the LSN:Ce phosphor (*i.e.*, 1:2, 1:1, 2:3 and 2:1) were evaluated. As shown in Fig. 5a where the IQE of the glass converters are presented, all the glass converters, having the highest IQE of

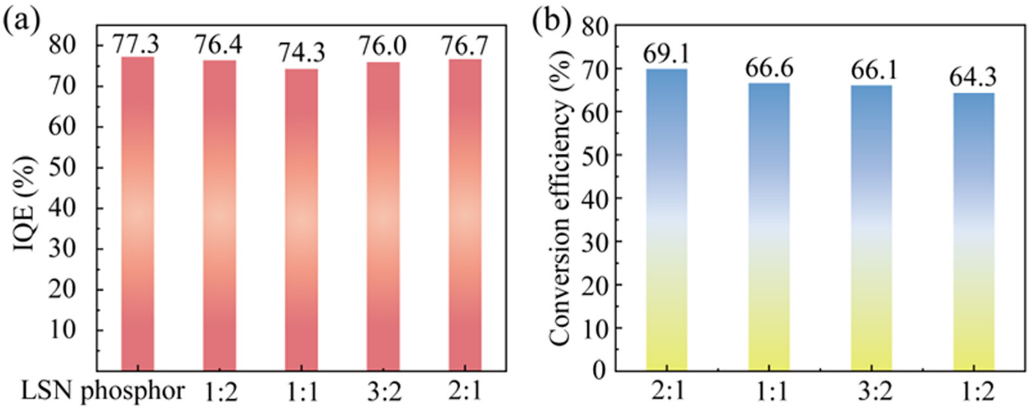

Fig. 5 (a) IQE and (b) conversion efficiency of the LSN-in-ZIF-62 glass converter with different glass-to-phosphor ratios.

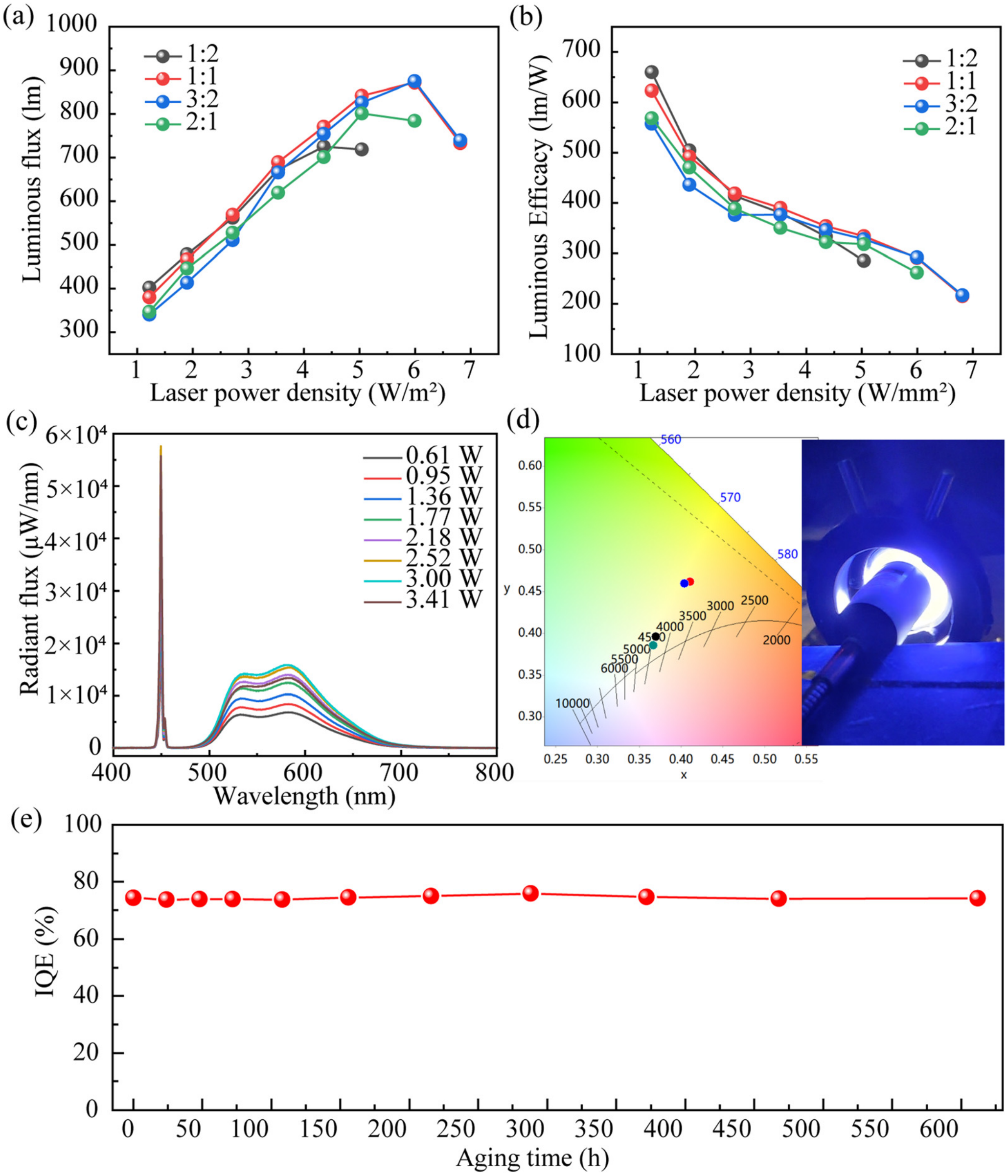

Fig. 6 Optical performance of the LSN-in-ZIF-62 glass converter with different glass-to-phosphor ratios. (a) and (b) Luminous flux and luminous efficacy as a function of the laser power density. (c) Emission spectra of the LSN-in-ZIF-62 glass converter (the glass-to-phosphor ratio is 1 : 1). (d) CIE color coordinates of the LSN-in-ZIF-62 glass converter with different glass-to-phosphor ratios and illumination image of white light from the LSN-in-ZIF-62 glass converter under excitation of blue laser. (e) Aging test of the LSN-in-ZIF-62 glass converter.

76.7%, exhibit a minimal IQE loss of ∼1% when compared to the original LSN:Ce powders. This strongly evidences that the LSN phosphor is protected by the oxygen-free ZIF-62 glass, and its IQE remains nearly unchanged after cofiring with the glass.

Owing to its high IQE and effective thermal management, the sandwich-structured LSN-in-ZIF-62 glass converter, with a glass-to-phosphor ratio of 1/1, allows preparing a laser-driven light source (CCT of 3860K, CRI of 60) with a maximum luminous flux of 872.2 lm and a luminous efficacy as high as 291.1 lm W^{-1} under excitation with a laser power density of 5.99 W mm^{-2} (Fig. 6a, b and Table S2, ESI†). As shown in Fig. 6c, the emission intensity of the LSN-in-ZIF-62 glass converter (ratio of the glass to phosphor is 1 : 1) monotonously increases as the incident laser power increases and reaches a maximum at 3 W. The light source illumination image of the LSN-in-ZIF-62 glass converter under excitation of blue laser is shown in Fig. 6d. Moreover, the calculated conversion efficiency of the glass converters remains high and varies in the range of 64–69% (Fig. 5b). Finally, the aging test of the LSN-in-ZIF-62 glass converter was investigated under 85 °C water vapor (Fig. 6e). The glass converter can still maintain a very high IQE more than 99% of its initial value even after aging for 612 hours, indicating that this novel glass converter possesses a long-term optical stability.

The protection mechanism of the LSN phosphor by the ZIF-62 glass is illustrated in Fig. 7a. In addition, owing to superior thermal conductivity and high transmittance of the sapphire substrate, the

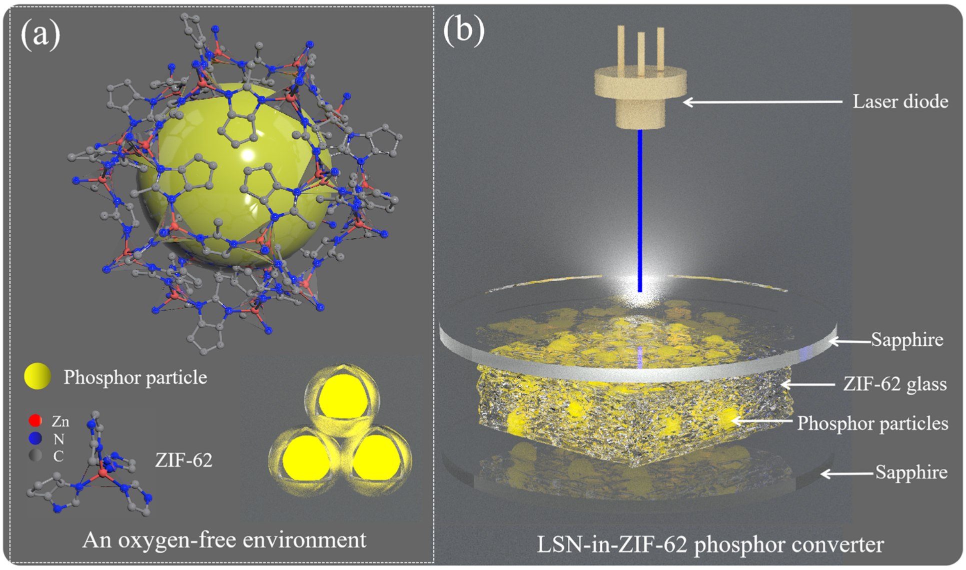

Fig. 7 (a) Mechanism of the organic–inorganic glass ZIF-62 providing an oxygen-free sintering environment for protecting LSN:Ce phosphors. (b) Schematic of the laser-driven sandwich-structured LSN-in-ZIF-62 phosphor converter.

Table 1 Optical properties of LSN-based color converters under laser irradiation

Samples	Luminous flux/lm	Luminous efficiency/lm W^{-1}	Saturation threshold/W mm^{-2}	Ref.
LSN-PiG film	1076	166.05	12.9	12
LSN-PiG film	376.1	158	2.39 (W)	24
LSN-PiG	209	145.91	1.44	23
LSN-Al_2O_3-PiG film	3120	130	23.08	22
LSN PiGF@diamond	5602	102.04	21.96	40
LSN-in-ZIF-62 glass	872.2	291.1	5.99	This work

sandwich-structured LSN-in-ZIF-62 glass converter can mitigate the direct impact of high-density photons on the glass converter with effective thermal management under laser excitation (Fig. 7b).

Table 1 summarizes the optical properties of some LSN-based PiG bulks or films under blue laser excitation. As observed, the LSN-in-ZIF-62 glass converter shows the highest luminous efficiency of 291.1 lm W^{-1} and a luminous flux of 872.2 lm even pumped by blue laser diodes with a small powder density of 5.99 W·mm^{-2}. These interesting results are ascribed to the high IQE preserved by using the ZIF-62 glass and the strong thermal management by using the sapphire substrate, which enable relatively high luminous flux and luminous efficacy under low-power-density of LD excitation, which is suitable for the low-power laser-driven lighting and displays, as well as high-power LED lighting applications.

4. Conclusion

In this work, an LSN-in-ZIF-62 glass converter has been designed and prepared by cofiring nitride phosphors with the OIHG at temperatures lower than 400 °C. The oxygen-free sintering environment provided by the ZIF-62 glass enabled the protection of the nitride phosphor particles from oxidation, and the internal quantum efficiency and photoluminescence spectra of phosphors almost remained unchanged after cofiring with the OIHG. The sandwich-structured LSN-in-ZIF-62 glass converter, constructed by using the sapphire substrates, showed enhanced thermal stability and allowed creating laser-driven white light with a luminous flux of 872.2 lm and a luminous efficacy of 291 lm W^{-1} when coupled to blue laser diodes with a power density of 5.99 W·mm^{-2}. This work offers a viable method to design efficient nitride phosphor converters suitable for low-power laser-driven lighting as well as high-power LED lighting applications or projection applications.

Author contributions

Taoli Deng: data curation, formal analysis, methodology, investigation, and writing – original draft. Zan Ding: methodology and formal analysis. Shuang Zheng: investigation. Rong-Jun Xie: conceptualization, methodology, writing – review & editing, supervision, and funding acquisition.

Data availability

The data supporting this article have been included as part of the ESI.†

Conflicts of interest

There is no conflict to declare.

Acknowledgements

This work is supported by the National Key Research and Development Program (MOST, 2022YFE0108800) and the Major Science and Technology Projects of Xiamen Science and Technology Bureau (No. 3502Z20231050).

Notes and references

1 S. X. Li, L. Wang, N. Hirosaki and R.-J. Xie, *Laser Photonics Rev.*, 2018, **12**, 1800173.

2 Y. G. Cao, R.-J. Xie, Q. L. Liu and X. Y. Chen, *Appl. Phys. Lett.*, 2022, **121**, 150401.

3 P. Hu, Y. F. Liu, P. Sun, Z. H. Luo and J. Jiang, *Adv. Opt. Mater.*, 2024, **12**, 2401672.

4 S. X. Liao, S. L. Jin, T. Pang, S. S. Lin, Y. H. Zheng, R. H. Chen, G. Y. Xi, X. Y. Li, B. Zhuang, F. Huang and D. Q. Chen, *Adv. Funct. Mater.*, 2024, **34**, 2307761.

5 T. L. Deng, D. Halmurat, Z. T. Shen, T. Y. Yan, S. X. Li, L. Wang and R.-J. Xie, *Laser Photonics Rev.*, 2023, **17**, 2300240.

6 C. C. Yang, X. Y. Zhang, J. Kang, C. Wei, P. F. Sang, S. H. Lin, B. H. Sun, J. T. Fan, B. X. Jiang, Y. Li, X. R. Chen, J. Xu, H. Chen and L. Zhang, *J. Mater. Sci. Technol.*, 2023, **166**, 1–20.

7 J. D. Zhang, H. S. Yang, Y. J. Zhang, X. D. Liu, Y. Q. Zhang, Y. Y. Liang, H. Li, B. Ma, X. J. Liang and W. D. Xiang, *Appl. Phys. Lett.*, 2021, **119**, 023301.

8 G. Z. Li, Q. W. Pan, Z. H. Zhou, R. R. Gu, H. Zhang, X. J. Huang, G. P. Dong and X. D. Xiao, *Adv. Opt. Mater.*, 2023, **11**, 2203028.

9 X. Y. Zhang, P. F. Sang, C. Wei, S. H. Lin, J. Kang, Y. B. Li, B. H. Sun, Y. Li, F. A. Selim, C. M. Zhou, T. Y. Zhou, S. W. Chen, C. F. Shi, W. Strek, H. Chen and L. Zhang, *J. Mater. Chem. C*, 2024, **12**, 6046–6055.

10 S. X. Li, Q. Q. Zhu, L. Wang, D. M. Tang, Y. J. Cho, X. J. Liu, N. Hirosaki, T. Nishimura, T. Sekiguchi, Z. R. Huang and R.-J. Xie, *J. Mater. Chem. C*, 2016, **4**, 8197–8205.

11 H. X. Chen, T. Lin, F. Huang, S. X. Li, X. Y. Tang and R.-J. Xie, *Adv. Opt. Mater.*, 2022, **10**, 2200836.

12 S. H. You, S. X. Li, P. Zheng, T. L. Zhou, L. Wang, L. H. Liu, N. Horisaki, F. F. Xu and R.-J. Xie, *Laser Photonics Rev.*, 2019, **13**, 1800216.

13 S. H. You, S. X. Li, Y. C. Jia and R.-J. Xie, *Chem. Mater.*, 2020, **32**, 3631–3640.

14 C. Y. Wang, T. Takeda, O. M. Ten Kate and R.-J. Xie, *J. Mater. Chem. C*, 2016, **4**, 10358–10366.

15 L. Wang, R.-J. Xie, T. Suehiro, T. Takeda and N. Hirosaki, *Chem. Rev.*, 2018, **118**, 1951–2009.

16 R. D. Tian, Q. H. Wang, S. X. Li, T. L. Zhou and R.-J. Xie, *J. Mater. Sci. Technol.*, 2025, **210**, 179–187.

17 S. X. Li, L. Wang, N. Hirosaki and R.-J. Xie, *Laser Photonics Rev.*, 2018, **12**, 1800173.

18 Q. Q. Zhu, X. J. Wang, L. Wang, N. Hirosaki, T. Nishimura, Z. F. Tian, Q. Li, Y. Z. Xu, X. Xu and R.-J. Xie, *J. Mater. Chem. C*, 2015, **3**, 10761–10766.

19 F. C. Xu, H. S. Yang, Y. J. Zhang, X. D. Liu, Y. Q. Zhang, L. S. Wang, Z. Wang, X. J. Liang, P. C. Qian and W. D. Xiang, *J. Alloys Compd.*, 2021, **887**, 161301.

20 S. X. Tao, Y. H. Ping, F. F. Huang, Y. J. Hua, P. Qiao, Y. G. Li, Z. C. Xu and H. P. Ma, *Ceram. Int.*, 2023, **49**, 19606–19614.

21 T. Lin, H. X. Chen, S. X. Li, L. Wang, F. Huang and R.-J. Xie, *Chem. Eng. J.*, 2022, **444**, 136591.

22 M. H. Huang, Q. Q. Zhu, S. X. Li, Y. Zhai, H. Zhang, L. Wang and R.-J. Xie, *J. Mater. Chem. C*, 2023, **11**, 488–496.

23 L. Xu, L. H. Wang, S. Y. Bao, Y. Wang, J. D. Zhang, Y. Y. Liang, X. J. Liang, Q. Chen and W. D. Xiang, *Ceram. Int.*, 2022, **48**, 23955–23962.

24 Z. K. Yu, J. Z. Zhao, J. X. Liu, Y. Mou, M. X. Chen and Y. Peng, *Ceram. Int.*, 2022, **48**, 36531–36538.

25 F. Du, W. D. Zhuang, R. H. Liu, Y. H. Liu, J. Y. Zhong, W. Gao, K. Chen, L. Chen, K. Kato and K. Lin, *RSC Adv.*, 2016, **6**, 77059–77065.

26 T. L. Deng, L. H. Huang, S. X. Li, Q. Q. Zhu, L. Wang, T. Takeda, H. Naoto and R.-J. Xie, *Laser Photonics Rev.*, 2022, **16**, 2100722.

27 A. Qiao, T. D. Bennett, H. Z. Tao, A. Krajnc, G. Mali, C. M. Doherty, A. W. Thornton, J. C. Mauro, G. N. Greaves and Y. Z. Yue, *Sci. Adv.*, 2018, **4**, eaao6827.

28 M. A. Ali, X. F. Liu, B. B. Xu, Y. Li, M. A. Mohamed, Y. Z. Yue and J. R. Qiu, *ACS Mater. Lett.*, 2022, **4**, 2613–2621.

29 M. A. Ali, W. M. Winters, M. A. Mohamed, D. Z. Tan, G. J. Zheng, R. S. Madsen, O. V. Magdysyuk, M. Diaz-Lopez, B. Cai, N. Gong, Y. J. Xu, I. V. Hung, Z. H. Gan, S. Sen, H. T. Sun, T. D. Bennett, X. F. Liu, Y. Z. Yue and J. R. Qiu, *Angew. Chem., Int. Ed.*, 2023, **62**, e202218094.

30 J. J. Yan, C. W. Gao, S. B. Qi, Z. J. Jiang, L. R. Jensen, H. B. Zhan, Y. F. Zhang and Y. Z. Yue, *Nano Energy*, 2022, **103**, 107779.

31 M. A. Ali, X. F. Liu, H. T. Sun, J. J. Ren and J. R. Qiu, *Chem. Mater.*, 2022, **34**, 2476–2483.

32 H. Z. Tao, T. D. Bennett and Y. Z. Yue, *Adv. Mater.*, 2017, **29**, 1601705.

33 Y. J. Zhao, L. Y. Zhu, Y. Q. Kang, C.-H. Shen, X. Y. Liu, D. Jiang, L. Fu, O. Guselnikova, L. J. Huang, X. K. Song, T. Asahi and Y. Yamauchi, *ACS Nano*, 2024, **18**, 22404–22414.

34 X. D. Liu, E. R. Mei, Z. Z. Liu, J. Du, X. J. Liang and W. D. Xiang, *ACS Photonics*, 2021, **8**, 887–893.

35 J. Huang, J. J. Zhou, E. Jungstedt, A. Samanta, J. Linnros, L. A. Berglund and I. Sychugov, *ACS Photonics*, 2022, **9**, 2499–2509.

36 R. J. Lin, M. L. Chai, Y. H. Zhou, V. C. Chen, T. D. Bennett and J. W. Hou, *Chem. Soc. Rev.*, 2023, **52**, 4149–4172.

37 J. W. Hou, P. Chen, A. Shukla, A. Krajnc, T. S. Wang, X. M. Li, R. Doasa, L. H. G. Tizei, B. Chan, D. N. Johnstone, R. J. Lin, T. U. Schülli, I. Martens, D. Appadoo, M. S. Ari, Z. L. Wang, T. Wei, S. C. Lo, M. Y. Lu, S. C. Li,

E. B. Namdas, G. Mali, A. K. Cheetham, S. M. Collins, V. Chen, L. Z. Wang and T. D. Bennett, *Science*, 2021, **374**, 621–625.

38 O. Smirnova, R. Sajzew, S. J. Finkelmeyer, T. Asadov, S. Chattopadhyay, T. Wieduwilt, A. Reupert, M. Presselt, A. Knebel and L. Wondraczek, *Nat. Commun.*, 2024, **15**, 5079.

39 S. Li, R. Limbach, L. Longley, A. A. Shirzadi, J. C. Walmsley, D. N. Johnstone, P. A. Midgley, L. Wondraczek and T. D. Bennett, *J. Am. Chem. Soc.*, 2019, **141**, 1027–1034.

40 Z. K. Yu, J. Z. Zhao, Z. Z. Yang, Y. Mou, H. J. Zhang, R. P. Xu, Q. Wang, L. W. Zeng, L. Lei, S. S. Lin, H. Li, Y. Peng, D. Q. Chen and M. X. Chen, *Adv. Mater.*, 2024, **36**, 2406147.